

END-EFFECTOR STABILIZATION OF A WEARABLE ROBOTIC ARM USING TIME SERIES MODELING OF HUMAN DISTURBANCES

Vighnesh Vatsal
Cornell University
Ithaca, USA
vv94@cornell.edu

Guy Hoffman
Cornell University
Ithaca, USA
hoffman@cornell.edu

ABSTRACT

For a wearable robotic arm to autonomously assist a human, it has to be able to stabilize its end-effector in light of the human's independent activities. This paper presents a method for stabilizing the end-effector in planar assembly and pick-and-place tasks. Ideally, given an accurate positioning of the end effector and the wearable robot attachment point, human disturbances could be compensated by using a simple feedback control strategy. Realistically, system delays in both sensing and actuation suggest a predictive approach. In this work, we characterize the actuators of a wearable robotic arm and estimate these delays using linear models. We then consider the motion of the human arm as an autoregressive process to predict the deviation in the robot's base position at a time horizon equivalent to the estimated delay. Generating set points for the end-effector using this predictive model, we report reduced position errors of 19.4% (x) and 20.1% (y) compared to a feedback control strategy without prediction.

INTRODUCTION

We present a framework for stabilizing the end-effector of a wearable robotic arm, which is subject to disturbances arising from movements of the user's arm to which it is attached. The context of this work is the continued development of a wearable robotic "third arm" extending from a user's elbow intended for close range human-robot collaboration [1]. It aims to extend a user's reach, and provide the ability for tasks such as self-handovers, object manipulation, and bracing, as shown in Fig. 1. In this paper we investigate the use of human motion prediction

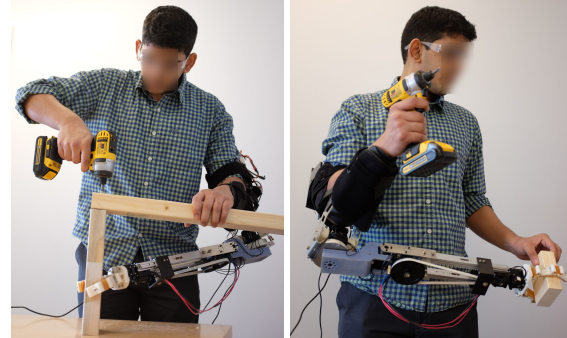


FIGURE 1: THE WEARABLE ROBOTIC ARM IN TWO ILLUSTRATIVE USAGE SCENARIOS: BRACING A WORK-PIECE (LEFT), AND SELF-HANOVER (RIGHT).

in a planar scenario where the end-effector needs to remain static, and compare this approach to feedback control without human motion prediction.

Related Work

The challenge of stabilizing a wearable robotic arm is related to that of manipulators rigidly mounted onto a mobile base. In typical mobile manipulators, however, both robotic components are controllable and as a result external disturbances from loads on either of them can be compensated for by generating combined cooperative motion plans for a specified task [2]. Force-based approaches, such as potential functions tracking the pro-

jection of the robot’s equilibrium point on the ground (Zero Moment Point) [3], and frequency-domain methods for vibration suppression [4] have been used to stabilize the mobile base and manipulator end-effector. A PID feedback controller with exponential position error weighting for the manipulator arm has been applied in scenarios where the mobile base is considered to be an independent system [5]. In our case, since the wearable robot is attached to a human arm which has structured but uncontrollable movements, the stabilization of the end-effector’s position needs to be performed by the manipulator alone.

This situation bears some similarity to the domain of hand-held robotic surgery devices, where physiological hand tremors have to be compensated for. One approach estimates tremors online by modeling them as truncated Fourier series, which are fed as an input to an open-loop controller for tool-tip position compensation [6]. Another approach involves modeling hand tremors as linear dynamic systems, with Kalman filtering for state estimation [7]. The hand tremor velocity estimate is considered to be a load disturbance, leading to a feed-forward control term added to a standard PID feedback controller. In our case, the actuators do no have feed-forward control capability, motivating a set-point prediction strategy to compensate for latency in sensing and actuation.

The most closely related work was presented in backpack mounted Supernumerary Robotic Limbs (SRL) involving human disturbance rejection through bracing [8]. Bracing involves the SRL grasping a structure in the environment to stabilize its user in a standing position. Human disturbances, in the form of postural sway, are modeled as external forces and torques acting on the SRL’s base. The pose estimation of the SRL base is improved using a bracing strategy generated by shaping the stiffness of the manipulator. Another scenario involves a force sensing-based drilling task in which the SRL holds a wooden piece steady while the wearer drills into it [9]. This approach used human-human demonstrations of the task, where the effects of the robot’s motions were condensed into force inputs, and the humans’ motions into tool-tip positions. An autoregressive moving-average process with exogenous inputs (ARMAX) model was used to predict the force required by the SRL to hold the workpiece stable during the task. Our scenario involves human arm movements on a similar scale as the leader’s hand motion with the SRL. However, instead of applying grasping forces to a static workpiece or the environment, the end-effector is stabilized in free space. We adopt a similar autoregressive approach for modeling only the motion of the human arm, with its effects on the end-effector compensated using feedback control.

Overview

In this work, we focus on a planar collaborative usage scenario (Fig. 2), where the wearable robotic arm retrieves workpieces and brings them to the user’s workspace, assists the user

in an assembly task, and stows workpieces at a desired location. The robotic arm grasps objects that are either handed over by the human in free space or under-constrained on a surface, preventing the adoption of a bracing strategy that requires a rigid connection with the environment.

We first describe the robot’s design and characterize the actuators used in this scenario. After estimating the delays in sensing and actuation that result in loss of performance of the robot in maintaining a steady pose, these delays are overcome using an autoregressive predictive model of human motion. Using this predictor as a set-point generator, the end-effector position error is reduced by an average of 19.4% in the x dimension and 20.1% cm in the y dimension, compared to direct feedback control.

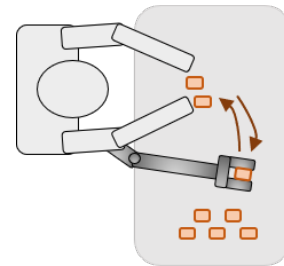


FIGURE 2: PLANAR COLLABORATIVE USAGE SCENARIO.

SYSTEM DESCRIPTION

In this section, we describe the kinematic structure of the robotic arm, as well as the planar setup with visual sensing for maintaining a steady robot end-effector pose.

Robot Design

The wearable robotic arm used in this work was developed through an iterative design process aimed at producing an SRL for close-range collaborative tasks [1]. Analysis of the robot’s biomechanical loads and workspace volume enhancement indicated that it would be useful for handover, pick-and-place, and bracing scenarios while remaining within ergonomic load limits [10].

The current model of the robot has five degrees of freedom (DoFs) plus a 1-DoF gripper (Fig. 3). Although this configuration is over-constrained, having 5-DoFs instead of six, it suffices for grasping in most pick-and-place scenarios. This trade-off is due to weight constraints, which are critical for an arm-mounted device. The robotic arm weighs ~ 1.5 kg, with a maximum reach of 0.63 m from the base joint. The robot’s kinematic structure is shown in Fig. 4, and the ranges of motion for each DoF are described using the Denavit-Hartenberg convention [11] in Table 1.

TABLE 1: D-H PARAMETERS FOR WEARABLE ROBOTIC ARM

	Degree of Freedom	α_i	$a_i(\text{m})$	$d_i(\text{m})$	θ_i
(1)	Horizontal panning	+90°	0	-0.08	(-180°, 180°)
(2)	Vertical pitching	+90°	0	0	(0°, 90°)
(3)	Length extension	0°	0	[0.33, 0.45]	180°
(4)	Wrist rotation	+90°	0	0.045	(-180°, 180°)
(5)	Wrist pitching	+90°	0	0	(0°, 180°)
(6)	End-effector	0°	0.135	0	0°

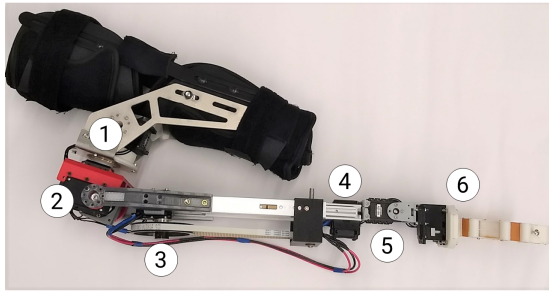


FIGURE 3: CURRENT PROTOTYPE OF THE WEARABLE ROBOTIC ARM WITH 5-DOFs, AND A GRIPPER AS THE END-EFFECTOR.

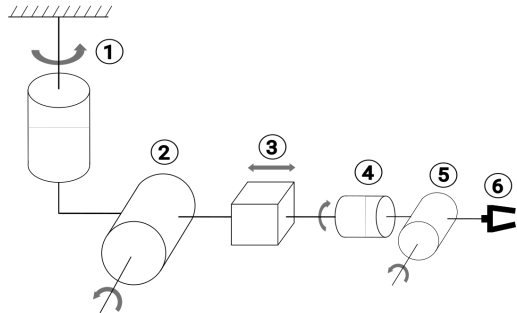


FIGURE 4: KINEMATIC DIAGRAM OF THE WEARABLE ROBOTIC ARM.

For the purposes of the scenario shown in Fig. 2, only the horizontal panning (DoF-1) and length extension (DoF-3) motions of the robotic arm are used.

Experimental Setup

In order to study the stabilization of the end-effector in the planar domain, we used the setup shown in Fig. 5. AprilTag fiducial markers [12] are placed on the robot's end-effector, and above the axis of DoF-1 (robot base) on the attachment point between the robot and the human arm. They are sensed with an Orbbec Astra stereo camera for vision-based position track-

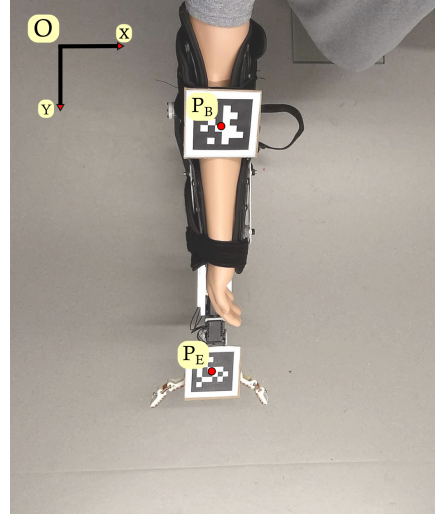


FIGURE 5: SYSTEM SETUP.

ing of these two points. The field of view of this setup is sufficient for small movements of the human arm (~15 cm), but may not be suitable for capturing large deviations. Fig. 5 shows the camera coordinate system $O = (x, y)$, with base coordinates $P_B = (x_B, y_B)$, and end-effector coordinates $P_E = (x_E, y_E)$. Given a detected deviation in the base position $(\Delta x_B, \Delta y_B)$, the new joint reference angle Θ_1 for DoF 1, and length reference L_3 for DoF-3, are computed using the 2-D Inverse Kinematics (IK) equation:

$$\begin{bmatrix} \Theta_1 \\ L_3 \end{bmatrix} = \begin{bmatrix} \tan^{-1}((y_E - y'_B)/(x_E - x'_B)) \\ \sqrt{(x_E - x'_B)^2 + (y_E - y'_B)^2} \end{bmatrix} \quad (1)$$

where $(x'_B, y'_B) = (x_B + \Delta x_B, y_B + \Delta y_B)$. In the current design of the robotic arm, length extension is achieved with a rack-and-pinion mechanism, so that L_3 is linearly related to Θ_3 , the motor joint angle for DoF-3. Given the current robot morphology, deviations in L_3 can be compensated by the wearable robotic arm to within ~12 cm.

The challenge of wearable arm compensation and stabilization can be viewed as a PID control problem, as shown in Fig. 6.

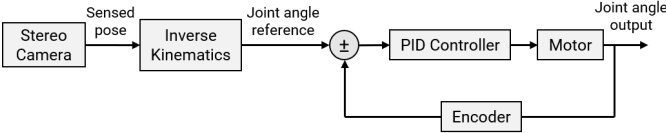


FIGURE 6: HIGH-LEVEL BLOCK DIAGRAM FOR FEEDBACK SYSTEM OF A MOTOR WITH PID CONTROLLER AND SETPOINT REFERENCE GENERATION THROUGH STEREO CAMERA SENSING.

The positions of the base and end-effector markers are sensed using fiducial markers. Joint angle set points for each motor are generated from these positions after applying equation (1), which are then tracked by built-in closed loop controllers in the servo motor hardware. Deviations in x and y coordinates of the end-effector are considered separately, since for the initial pose shown in Fig. 5, the x coordinate is predominantly affected by DoF-1, and y coordinate by DoF-3.

ESTIMATION OF MOTOR PERFORMANCE, HUMAN MOVEMENT, AND DELAYS

To analyze whether the robotic arm is able to compensate for human disturbances using the feedback control strategy shown in Fig. 6, we first perform a system characterization of the robot using transfer function models. We then conduct an analysis of the spectral properties of empirical human arm motion from data collected in our setup and compare them to the bandwidth of the motors. This is followed by the estimation of sensing and actuation delays using a transfer function model.

Motor Models

The robot's DoFs are actuated using ROBOTIS Dynamixel DC servo motors [13], with built-in velocity and position PID feedback controllers. Reference velocities for these DoFs are chosen such that the torque loads on the motors do not exceed 20% of their maximum ratings, as specified by the manufacturer for stable operation: 1.1 rad/s for DoF-1, and 3.0 rad/s for DoF-3, determined from preliminary trials.

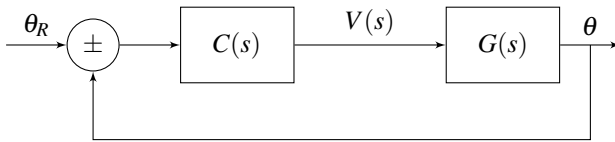


FIGURE 7: BLOCK DIAGRAM FOR MOTOR FEEDBACK CONTROL SYSTEM.

Characterization of the performance of these motors follows a system identification procedure similar to [14]. The feedback loop is modeled as a PID controller driving a DC motor (Fig. 7). The DC motor is modeled as an L-R circuit [15], with voltage $V(t)$ related to the inductance L , winding resistance R , and current $i(t)$ as $V(t) = Li(t) + Ri(t) + E(t)$. Here $E(t) = K_e\dot{\theta}(t)$ is the back-EMF generated by the rotation of the motor, dependent on the angular speed using the Back-EMF constant K_e . The motor torque $\tau(t)$ is proportional to the current $i(t)$ with torque constant K_t and acts on the mechanical elements of the motor with moment of inertia I and damping factor K_c , giving $\tau(t) = I\ddot{\theta}(t) + K_c\dot{\theta}(t) = K_t i(t)$.

Applying the Laplace transform to these equations, the plant transfer function $G(s)$ between reference angle $\theta(s)$ and voltage $V(s)$ is obtained:

$$G(s) = \frac{\theta(s)}{V(s)} = \frac{K_t}{(sL+R)(s^2I+sK_c)+sK_eK_t} \quad (2)$$

The manufacturer-supplied PID parameters have a non-zero gain only for proportional position control, resulting in a controller transfer function of the form $C(s) = K_p$.

The closed-loop transfer function $P(s)$ between the motor angle θ and a reference signal θ_R for each DoF takes the form of a third-order system with no zeros:

$$P(s) = \frac{\theta(s)}{\theta_R(s)} = \frac{GC(s)}{1+GC(s)} = \frac{B_0}{A_0+A_1s+A_2s^2+s^3} \quad (3)$$

TABLE 2: MOTOR STEP RESPONSE CHARACTERISTICS

Parameter	DoF 1	DoF 3
Rise time (s)	0.133	0.294
Settling time (s)	0.539	0.489
Overshoot (%)	10.79	0.487
Peak time (s)	0.293	0.650
Bandwidth (Hz)	2.726	1.174

To find the parameters A_{0-2} and B_0 , we perform closed-loop step response tests with joint positions recorded from built-in motor encoders for typical reference signals given to these actuators during end-effector stabilization (Figs. 8, 9). They

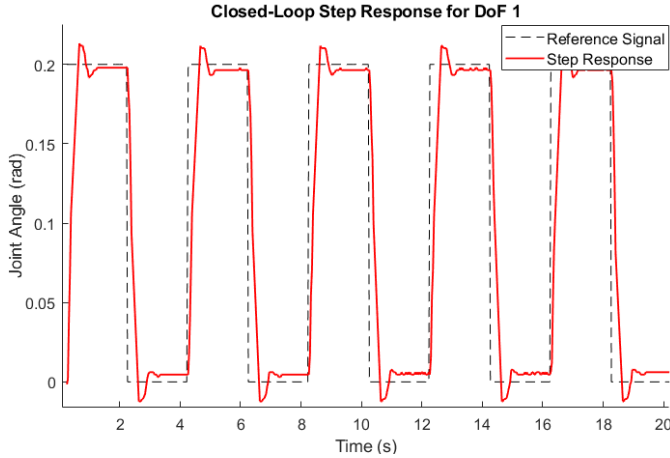


FIGURE 8: CLOSED-LOOP STEP RESPONSE FOR DOF-1 (HORIZONTAL PANNING) FOR A REFERENCE STEP SIGNAL OF AMPLITUDE 0.2 RAD, MEASURED USING ON-BOARD ENCODERS.

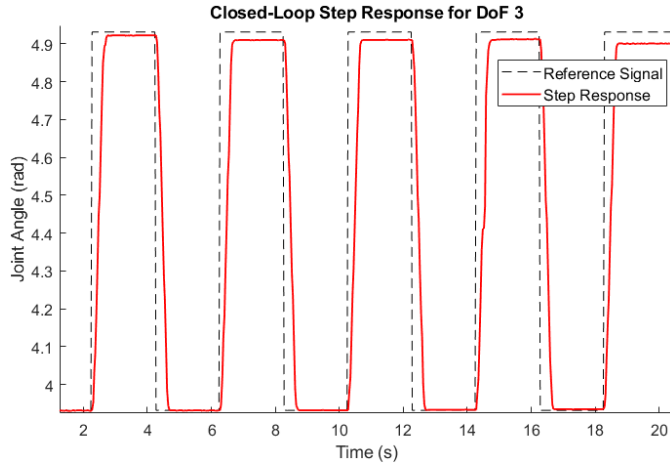


FIGURE 9: CLOSED-LOOP STEP RESPONSE FOR DOF-3 (LENGTH EXTENSION) FOR A JOINT ANGLE REFERENCE STEP SIGNAL OF AMPLITUDE 1 RAD, WHICH CORRESPONDS TO A CHANGE IN LENGTH OF ~7 CM.

are estimated using the Simplified Refined Instrumental Variable method for Continuous-time (SRIVC) model identification method [16]. The goodness of fit of these models is measured by a normalized root-mean-squared error (NRMSE) metric, which ranges from $(-\infty, 1]$, with 1 indicating a perfect fit. The NRMSE fit metric is 0.9169 for DoF-1 and 0.9543 for DoF-3. After model fitting, the step response characteristics for these motors are estimated (Table 2). The motors have reasonably fast responses, with bandwidths of ~2.7 Hz and ~1.2 Hz respectively, and settling within ~0.5 s to the maximum joint angle deviations likely to be

encountered in our scenario. The difference in performance is due to a higher-end Dynamixel MX-64 motor used for DoF-1, compared to a lower power MX-28 motor for DoF-3.

Human Arm Motion Data

Given the characterization of the motors, we now turn to the human arm motions that need to be compensated for, analyzing the spectral properties of a sample motion dataset.

Using the setup shown in Fig. 5, a dataset of $N = 3604$ points (x_B, y_B) is collected, of a wearer moving their arm about a mean position within an amplitude of ~15 cm, with the motors of the robotic arm held steady. The camera in our setup has a data collection rate of ~26 Hz. Fig. 10 shows an illustrative data sample.

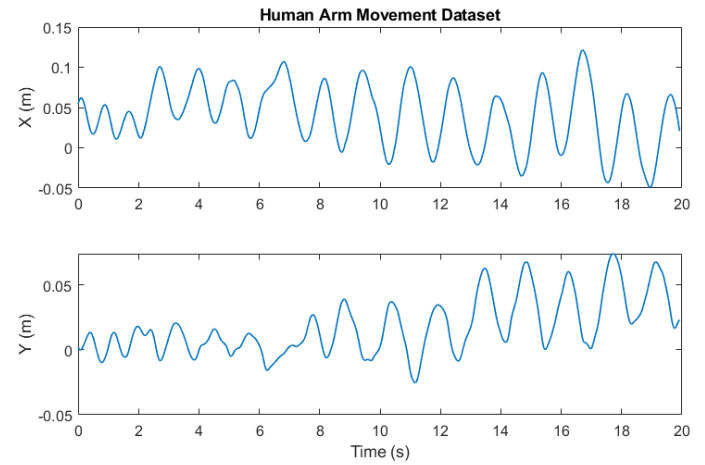


FIGURE 10: ILLUSTRATIVE PLOTS OF THE HUMAN ARM MOVEMENT DATASET: MOST MOTIONS ARE RESTRICTED TO WITHIN ~15 CM FROM THE STARTING POSITION.

The Fourier transforms of the x and y coordinates from the dataset show that the human arm motion while wearing the robotic arm is composed of frequencies largely below 1 Hz (Fig. 11). The bandwidth of the robot's actuators is greater than 1 Hz (Table 2). This indicates that the actuators should be able to compensate for most of the disturbances introduced at the robot's base by the human arm in a feedback control system as shown in Fig. 6. The effect of physiological tremors with frequencies of 10 Hz and higher is negligible, since their typical amplitudes are of the order of 0.1 mm [6].

Delay Estimation

While the above characterization of the human movement and motor properties suggests that a feedback control system

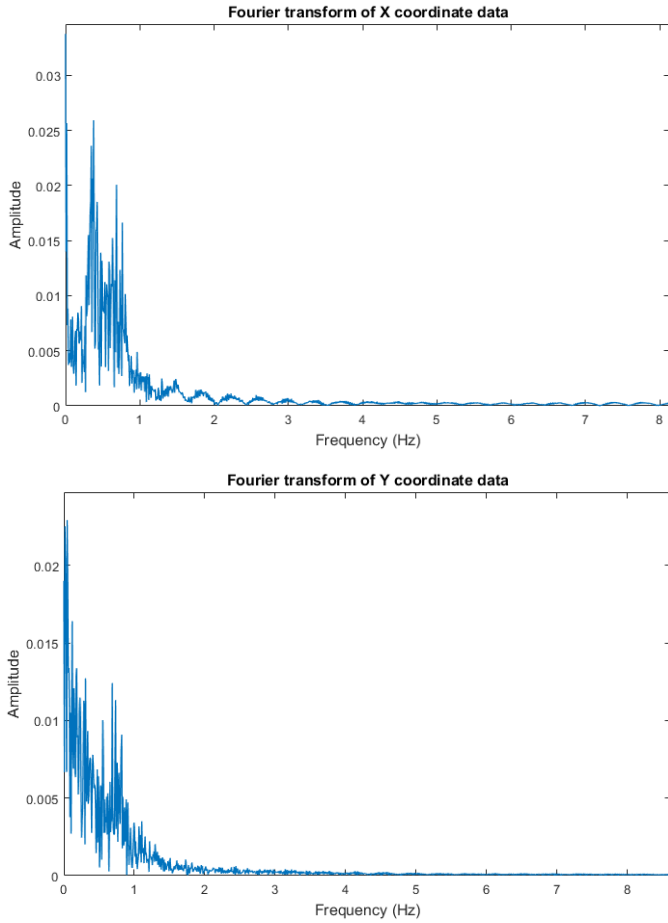


FIGURE 11: FOURIER TRANSFORM PLOTS OF ROBOT BASE POSITION (x_B, y_B) DATA.

would be able to compensate for human-generated disturbances, in practice the system has a mean error of about 5.9 cm in x and 3.7 cm in y using feedback control alone (Table 4).

This performance degradation is affected by delays stemming from a combination of latency in communication with the motors (rate of ~ 50 Hz), vision tracking system (rate of ~ 26 Hz), mechanical transmission delays, as well as nonlinear effects in the motors due to Coulomb and viscous friction [17]. Improving stabilization performance requires a predictive approach to account for these delays.

The aggregate effect of these delays can be identified using a closed-loop step response procedure. Since the motor response for DoF-3 has higher rise time and settling time, as well as lower bandwidth (Table 2), it will act as the limiting factor in terms of time delay. Therefore the third-order system in (3) for DoF-3 is augmented with a time delay term:

$$P(s) = \frac{\theta(s)}{\theta_R(s)} = \frac{e^{-\tau_d s} B_0}{A_0 + A_1 s + A_2 s^2 + s^3} \quad (4)$$

The step response is determined by tracking the visual markers for the same reference inputs given in Fig. 9, and computing the joint angle Θ_3 by applying the IK equation (1). This allows for the estimation of the time delay τ_d between the motor's internal response and detection of the same movement by the camera. As before, the SRIVC system identification procedure is applied to step response tests for DoF-3 (Fig. 12), and the delay τ_d is found to be 76.48 ms, with an NRMSE model fit of 0.8479. Compensating for this delay requires a prediction of two time steps into the future for a sampling rate of ~ 26 Hz of the camera (sampling period of ~ 38.5 ms).

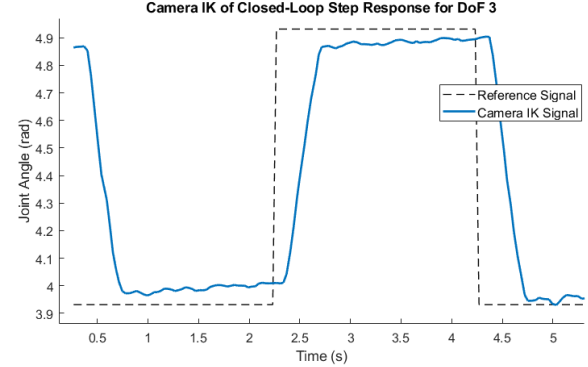


FIGURE 12: CLOSED-LOOP STEP RESPONSE OF DOF 3 MEASURED BY APPLYING IK EQUATION TO DATA FROM THE STEREO CAMERA. THE DELAY τ_d IS ESTIMATED BY FITTING A LINEAR MODEL TO THIS DATA.

AUTOREGRESSIVE MODEL

After estimating the delay present in our system, we aim to improve end-effector stabilization performance by predicting the robot's base position movements over the time horizon equal to the delay. We do so by learning an autoregressive predictive model for the human arm motion.

As a first assumption, similar to [9], the deviations in the x and y coordinates of the human arm movement are modeled as discrete univariate time series composed of a combination of Auto Regressive (AR) and Moving Average (MA) terms (“ARMA”), with no exogenous inputs:

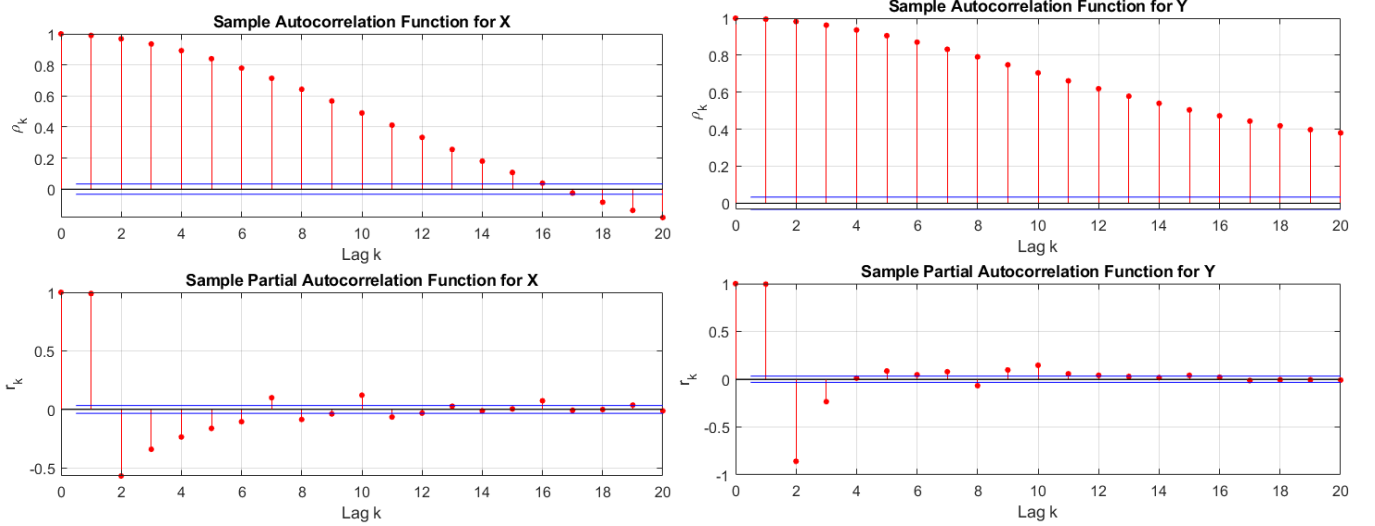


FIGURE 13: AUTOCORRELATION FUNCTIONS ρ_k AND r_k FOR x AND y COORDINATE DATA FOR LAGS $k = 1, \dots, 20$ WITH TWO STANDARD ERROR CONFIDENCE BOUNDS. r_k DROPS OFF MUCH FASTER THAN ρ_k , INDICATING A PREDOMINANCE OF AR TERMS.

$$x_t = C + \sum_{i=1}^p A_i x_{t-i} + \sum_{j=1}^q B_j \varepsilon_{t-j} \quad (5)$$

Here x_t is either the x or y position coordinate error, ε_t is a white noise series with zero mean and σ^2 variance, assumed to be normally distributed. Past coordinates are included in this model up to p time steps, which is the order of the autoregression (AR) part, with coefficients A_i . Past white noise terms in the moving average (MA) part are included up to an order q , with coefficients B_j . The constant term C is assumed to be zero, since deviations are measured from an initial position. This model makes the assumption that x_t is stationary, i.e. its expected value and variance are independent of time. This property is verified to hold true for our dataset using the augmented Dickey-Fuller hypothesis test [18].

In the next step, we investigate which of the terms, AR or MA, are dominant in the data. The dominance of either term would indicate that a simplified model could be adopted instead of a full ARMA model. To do so, we compare the sample autocorrelation function, ρ_k with the sample partial autocorrelation function, r_k . ρ_k is the correlation between sample points x_t and x_{t-k} :

$$\rho_k = \text{Corr}(x_t, x_{t-k}) = \frac{\text{Cov}(x_t, x_{t-k})}{\text{Var}(x_t)} \quad (6)$$

The partial autocorrelation r_k measures the correlation between x_t and x_{t-k} after discounting for the effects of all intermediate lags $x_{t-1}, \dots, x_{t-k+1}$. This measures the direct dependence between a data point and its lagged value, as opposed to ρ_k , which encodes the dependence of intermediate terms as well.

$$r_k = \text{Corr}(x_t - \hat{x}_t, x_{t-k} - \hat{x}_{t-k}) \quad (7)$$

Here \hat{x}_t and \hat{x}_{t-k} are the best linear projections of x_t and x_{t-k} onto the intermediate terms using least-squares regression.

Fig. 13 shows that ρ_k decays at a much lower rate than r_k for both coordinates, indicating that a data point x_t depends more heavily on past points x_{t-k} rather than past white noise terms ε_{t-k} [19]. This allows for the simplification of the ARMA(p,q) model into a purely autoregressive AR(p) model:

$$x_t = \sum_{i=1}^p A_i x_{t-i} + \varepsilon_t \quad (8)$$

To find the order p of this AR(p) model, we apply the Bayesian Information Criteria (BIC), which optimizes a log-likelihood goodness of fit while penalizing more complex models [19]:

$$\text{BIC} = -2\log(L) + (p+1)\log(N) \quad (9)$$

TABLE 3: Autoregressive AR(p) Model Parameters

Coordinate	Parameter	Value
x	A_i	[1.2619, -0.0722, -0.0686, 0.0050, -0.0406, -0.2326, 0.2070, -0.0372, -0.1961, 0.1999, -0.0510]
	σ^2	6.6439×10^{-5}
y	A_i	[1.6304, -0.3713, -0.2085, -0.1065, 0.0342, -0.0755, 0.2587, -0.1537, -0.1247, 0.0516, 0.0598]
	σ^2	8.0532×10^{-6}

Here L is the likelihood function, p is the order of the AR process, and N is the number of samples. The order $p = 11$ is found to have minimum BIC for both coordinates. The model parameters A_i and white noise variance σ^2 for these AR($p=11$) processes are estimated using the Yule-Walker method [20], and listed in Table 3.

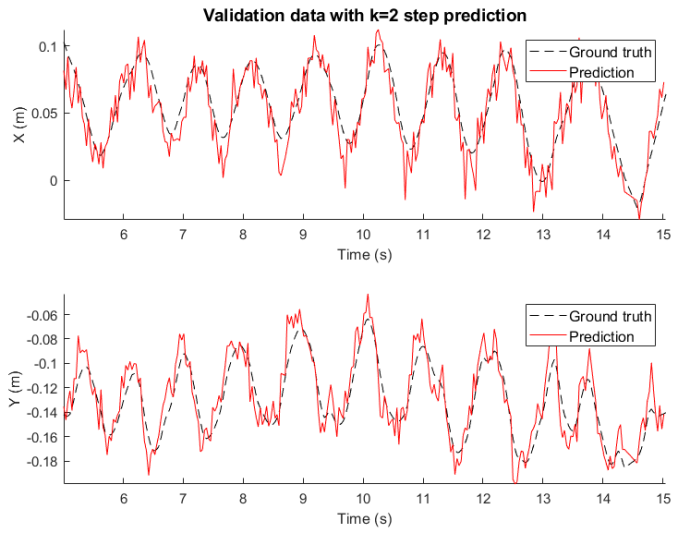


FIGURE 14: SAMPLE OF HUMAN ARM MOTION PREDICTION DATA (RED), ALIGNED WITH GROUND TRUTH (BLACK).

This model is tested on a validation dataset of $N=1050$ points collected in the same setup (Fig. 5), for predictions $k=2$ time steps into the future, which should compensate for system delays of ~ 77 ms. This two-step prediction matches the ground truth data well (Fig. 14), having mean absolute errors of 1.53 cm and 0.73 cm respectively in x and y coordinates, with standard deviations of 1.87 cm and 0.89 cm.

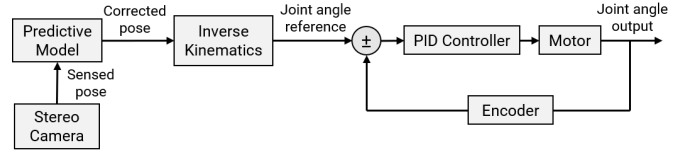


FIGURE 15: HIGH-LEVEL BLOCK DIAGRAM FOR FEEDBACK CONTROL WITH THE PREDICTIVE AR MODEL USED FOR GENERATING REFERENCE SETPOINTS FROM SENSED STEREO CAMERA DATA.

RESULTS

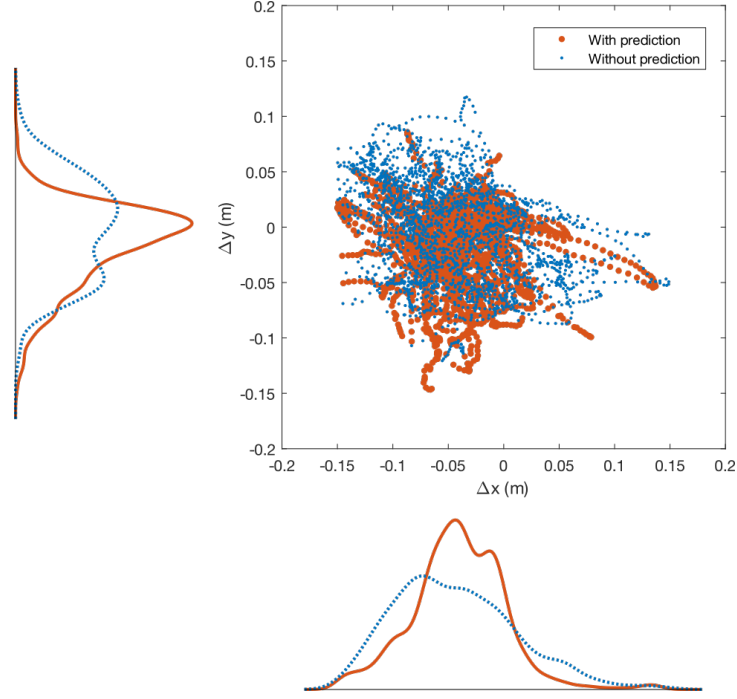
Having obtained an autoregressive predictive model for human arm motion, its performance is compared to the case without prediction when applied to end-effector stabilization.

An overview of the feedback control strategy without prediction is shown in Fig. 6, with the IK equation (1) being used to generate joint angle setpoints. This strategy is augmented with an AR model predicting human arm motion in order to compensate for delays in the system, illustrated in Fig. 15 with an additional block for the predictive model after visual sensing.

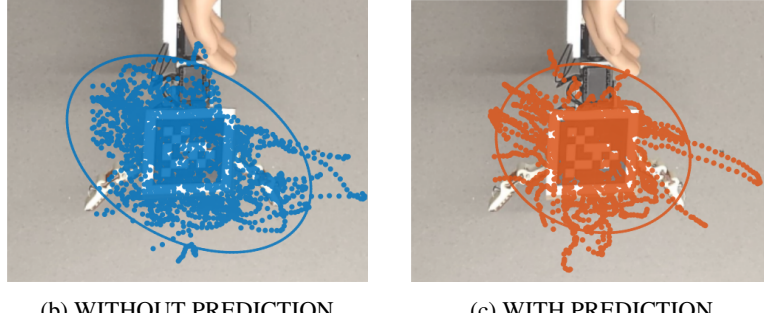
TABLE 4: Deviation of End-Effector with and without prediction

Quantity	Mean (cm)	Std. Dev. (cm)
$ \Delta x _{\text{nopred}}$	5.921	3.732
$ \Delta x _{\text{pred}}$	4.765	3.398
$ \Delta y _{\text{nopred}}$	3.706	2.402
$ \Delta y _{\text{pred}}$	2.959	2.768

Both these strategies are implemented independently, collecting $N=2312$ data points without prediction, and $N=2750$ points with the AR predictive model in use. The resulting scatter plots of end-effector pose along with their kernel density estimates are shown in Fig. 16. Table 4 reports mean and standard deviations of the absolute errors in displacement from the starting



(a) SCATTER PLOTS AND GAUSSIAN KERNEL DENSITY ESTIMATES OF END-EFFECTOR POSITION ERROR



(b) WITHOUT PREDICTION

(c) WITH PREDICTION

FIGURE 16: COMPARISON OF END-EFFECTOR POSITION ERRORS WITH (ORANGE) AND WITHOUT (BLUE) THE PREDICTIVE AR MODEL: (a) THE PREDICTIVE MODEL RESULTS IN LOWER MEAN POSITION ERROR IN x AND y COORDINATES; (b), (c) SHOW THE INDIVIDUAL ERROR SCATTER PLOTS WITH 95% CONFIDENCE REGIONS.

pose with only feedback control ($|\Delta x|_{noper}$ and $|\Delta y|_{noper}$), and feedback control along with the predictive AR model ($|\Delta x|_{pred}$ and $|\Delta y|_{pred}$). Position errors are reduced by about 1.15 cm (19.4%) in the x coordinate and 0.75 cm (20.1%) in the y coordinate. This difference in performance improvement is likely due to a higher power motor used for DoF-1, that primarily affects the x coordinate.

CONCLUSION

This paper presented a method for stabilizing the end-effector of a wearable robotic arm by accounting for human-induced disturbances in its base position and delays introduced in the sensing and actuation. An autoregressive model of the human arm motion yielded accurate predictions ~ 77 ms into the future, allowing for improved stabilization performance.

Although such predictions may not be necessary in mobile manipulation settings with powerful actuators and high-speed cameras, weight considerations for wearable robotic devices im-

pose a cap on the performance of motors given present power density limitations. End-effector stabilization is achieved here using off-the-shelf components for sensing and actuation, in a simplified 2-D workspace with a limited field of view, accounting only for situations with small movements of the human arm. Larger movements, e.g. while walking with the robot, would require more extensive sensing, and a full kinematic predictive model of human body motion, which may not be captured by a time series approach, instead requiring a supervised learning method with more training data.

Within a restricted workspace, the human arm model presented here can be adapted for predicting the full 6-D pose of the robot's base. We aim to extend this work to stabilizing spatial trajectories of the end-effector while rejecting disturbances from the wearer's arm motion. This forms part of a broader effort into wearable human-robot collaboration, involving the development of high-level controllers for generating robot behaviors in close-range collaborative tasks.

ACKNOWLEDGMENT

This work was supported by the National Science Foundation under NRI Award no. 1734399.

REFERENCES

- [1] Vatsal, V., and Hoffman, G., 2017. "Wearing your arm on your sleeve: Studying usage contexts for a wearable robotic forearm". In Robot and Human Interactive Communication (RO-MAN), 2017 26th IEEE Int. Symposium on, pp. 974–980.
- [2] Seraji, H., 1995. "Configuration control of rover-mounted manipulators". In Proceedings of 1995 IEEE International Conference on Robotics and Automation, Vol. 3, IEEE, pp. 2261–2266.
- [3] Huang, Q., and Sugano, S., 1995. "Manipulator motion planning for stabilizing a mobile-manipulator". In Proceedings 1995 IEEE/RSJ International Conference on Intelligent Robots and Systems, Vol. 3, IEEE, pp. 467–472.
- [4] Abeygunawardhana, P. K., and Murakami, T., 2010. "Vibration suppression of two-wheel mobile manipulator using resonance-ratio-control-based null-space control". *IEEE Transactions on Industrial Electronics*, **57**(12), pp. 4137–4146.
- [5] Ram, R., Pathak, P., and Junco, S., 2018. "Trajectory control of a mobile manipulator in the presence of base disturbance". *Simulation*, p. 0037549718784186.
- [6] Riviere, C. N., Gangloff, J., and De Mathelin, M., 2006. "Robotic compensation of biological motion to enhance surgical accuracy". *Proceedings of the IEEE*, **94**(9), pp. 1705–1716.
- [7] Becker, B. C., MacLachlan, R. A., and Riviere, C. N., 2011. "State estimation and feedforward tremor suppression for a handheld micromanipulator with a kalman filter". In 2011 IEEE/RSJ International Conference on Intelligent Robots and Systems, IEEE, pp. 5160–5165.
- [8] Parietti, F., and Asada, H. H., 2013. "Dynamic analysis and state estimation for wearable robotic limbs subject to human-induced disturbances". In 2013 IEEE International Conference on Robotics and Automation, IEEE, pp. 3880–3887.
- [9] Llorens-Bonilla, B., Parietti, F., and Asada, H., 2012. "Demonstration-based control of supernumerary robotic limbs". In Intelligent Robots and Systems (IROS), 2012 IEEE RSJ International Conference on, pp. 7–12.
- [10] Vatsal, V., and Hoffman, G., 2018. "Design and analysis of a wearable robotic forearm". In 2018 IEEE International Conference on Robotics and Automation (ICRA), IEEE, pp. 1–8.
- [11] Hartenberg, R. S., and Denavit, J., 1955. "A kinematic notation for lower pair mechanisms based on matrices". *J. of Appl. Mechanics*, **77**(2), pp. 215–221.
- [12] Olson, E., 2011. "Apriltag: A robust and flexible visual fiducial system". In 2011 IEEE International Conference on Robotics and Automation, IEEE, pp. 3400–3407.
- [13] Robotis. Dynamixel motor datasheets, retrieved 13-Mar-2019 from <http://en.robotis.com/>.
- [14] Wada, T., Ishikawa, M., Kitayoshi, R., Maruta, I., and Sugie, T., 2009. "Practical modeling and system identification of r/c servo motors". In Control Applications,(CCA) & Intelligent Control,(ISIC), 2009, IEEE, pp. 1378–1383.
- [15] Bolton, W., and Naidu, D., 1996. "Mechatronics: Electronic control systems in mechanical engineering". *Mechtronics*, **4**(6), pp. 491–493.
- [16] Young, P., and Jakeman, A., 1980. "Refined instrumental variable methods of recursive time-series analysis part iii. extensions". *International Journal of Control*, **31**(4), pp. 741–764.
- [17] Schwarz, M., and Behnke, S., 2013. "Compliant robot behavior using servo actuator models identified by iterative learning control". In Robot Soccer World Cup, Springer, pp. 207–218.
- [18] Dickey, D. A., and Fuller, W. A., 1979. "Distribution of the estimators for autoregressive time series with a unit root". *Journal of the American statistical association*, **74**(366a), pp. 427–431.
- [19] Box, G. E., Jenkins, G. M., Reinsel, G. C., and Ljung, G. M., 2015. *Time series analysis: forecasting and control*. John Wiley & Sons.
- [20] Friedlander, B., and Porat, B., 1984. "The modified yule-walker method of arma spectral estimation". *IEEE Transactions on Aerospace and Electronic Systems*(2), pp. 158–173.